Enhanced axial and lateral resolution using stabilized pulses

Shujie Chen and Kevin J. Parker*
University of Rochester, Department of Electrical and Computer Engineering, Rochester, New York, United States

Abstract. Ultrasound B-scan imaging systems operate under some well-known resolution limits. To improve resolution, the concept of stable pulses, having bounded inverse filters, was previously utilized for the lateral deconvolution. This framework has been extended to the axial direction, enabling a two-dimensional deconvolution. The modeling of the two-way response in the axial direction is discussed, and the deconvolution is performed in the in-phase quadrature data domain. Stable inverse filters are generated and applied for the deconvolution of the image data from Field II simulation, a tissue-mimicking phantom, and *in vivo* imaging of a carotid artery, where resolution enhancement is observed. Specifically, in simulation results, the resolution is enhanced by as many as 8.75 times laterally and 20.5 times axially considering the −6-dB width of the autocorrelation of the envelope images. [DOI: 10.1117/1.JMI.4.2.027001]

Keywords: superresolution; ultrasound images; resolution enhancement; deconvolution; *Z*-transform; stable inverse filters.

Paper 17061R received Mar. 7, 2017; accepted for publication Apr. 17, 2017; published online May 8, 2017.

1 Introduction

A variety of mathematical models and techniques have been applied to improve the resolution of imaging systems. For ultrasound imaging, the methods to achieve a better resolution can be categorized into two types:[1,2] more sophisticated imaging techniques and better postprocessing algorithms. The former tries to get more information at the imaging stage using approaches such as spatial/frequency compounding,[3,4] pulse coding/compression,[5–8] synthetic aperture imaging,[9] and harmonic imaging,[10,11] while the latter utilizes signal processing techniques to recover as much information as possible from the precaptured image data. Theories, such as time reversal and multiple signal classification[12–14] based on the decomposition of the time reversal operator,[15,16] have been used to resolve the scatterers or extended targets, e.g., breast microcalcifications.[17,18] However, the most common approach used in the postprocessing stage is deconvolution.

Under the assumption of linear propagation, weak scattering (or Born approximation), and ignoring attenuation and multipath effects, the interaction of the propagating pulse and the scatterers or reflectors can be formulated into a convolution model.[19–24] Based on such a model, deconvolution methods can be applied to recover the ground truth and thus, improve the image resolution. There are blind and nonblind deconvolution methods. Blind deconvolution algorithms[2,25–34] improve the resolution by jointly estimating the point spread function (PSF) and the reflection coefficients of tissue. On the other hand, nonblind deconvolution approaches utilize more prior information and are thus generally more specific for the imaging system and have better performance.[23,35–38]

Within the framework of nonblind deconvolution, a specific approach to superresolution imaging for pulse-echo systems was previously described for stabilized asymmetric pulses.[38] Our more recent paper treated the lateral deconvolution for symmetric stabilized pulses.[36] For symmetric double-sided functions (comprised of both causal and anticausal parts), the region of convergence for a stable system with an inverse will be an annulus that includes regions both inside and outside of the unit circle. Therefore, stabilized pulses are defined as realizable focal patterns and beam patterns that are continuous functions in the axial and transverse directions, such that when sampled, they have their *Z*-transform zeros positioned away from the unit circle. This corresponds to inverse filters that are stable in that they are limited in extent with bounded output. Such inverse filters are bounded and well behaved in the presence of noise, and proper design of the stabilized pulse, analyzed with the help of the *Z*-transform, can be an important part of a superresolution strategy.

In this paper, we extend the work to two-dimensional (2-D) (axial and lateral) resolution enhancement where stabilized beam patterns can be produced and sampled so as to have stable and useful inverse filters. We also explicitly treat the problem of scatterers positioned at subinteger shifts among the nominally sampled locations. Coherent deconvolution introduced previously in Ref. 36 may be performed in the two dimensions sequentially. Examples are provided from Field II[39,40] and ultrasound B-scans. We demonstrate that an axial deconvolution can be treated within the same general framework as lateral resolution, and resolution enhancement is possible in both axial and lateral dimensions.

2 Theory

2.1 *Pulse-Echo Convolution Model*

In conventional B-mode ultrasound imaging—assuming a narrowband transmission, weak scattering, and with some approximation—the classical convolution model gives us the

*Address all correspondence to: Kevin J. Parker, E-mail: kevin.parker@rochester.edu

2329-4302/2017/$25.00 © 2017 SPIE

relationship between the received radiofrequency (RF) data and the imaging configurations, which is derived based on the work of Prince and Links[41] as

$$\hat{r}(x,y,z) = r(x,y,z) *** p(x,y,z), \tag{1}$$

where x, y, and z are the coordinates in the lateral, the elevational, and the axial directions, respectively, k is the wave number, r is the reflection coefficient of the scatterers, $\hat{r}$ is the resulting image as the RF data, and $p(x,y,z)$ is the propagating pulse. We assume that $p(x,y,z)$ is separable and of the form

$$p(x,y,z) = \mathbf{e}^{jk(x^2+y^2)/z} s\left(\frac{x}{\lambda z}, \frac{y}{\lambda z}\right)^2 n_e\left(\frac{z}{c/2}\right) \sin(2kz+\phi), \tag{2}$$

where c is the speed of sound, $s(\cdot)^2$ is the round-trip lateral beam pattern, related to the Fourier transform of the apodization function in the transducer face, $n_e(2z/c)$ [or essentially $n_e(t)$ as $z = ct/2$] is the envelope of the axial propagating pulse with λ as its wavelength, ϕ is the initial phase, and the operator *** represents the three-dimensional convolution. This formulation suggests the separable PSF in the lateral and axial directions. Laterally, the Fourier transform relationship is utilized between the beam pattern at focus and the apodization weights. In the axial direction, the PSF is modeled as a modulated sinusoidal wave.

Under some conditions, a few simplifications can be applied. Let us assume that all scatterers lie in the $y = 0$ plane; this reduces the problem to a 2-D model. Further, the beam pattern is assumed to be relatively constant for some depth near the focus. Finally, the quadratic phase term can be neglected in the paraxial approximation or by adding additional time delay for each individual channel of the transducer. Under these assumptions, the received signal is modeled as a simple convolution

$$\hat{r}(x,z) = r(x,z) ** \left[s\left(\frac{x}{\lambda z_f}\right)^2 n_e\left(\frac{z}{c/2}\right) \sin(2kz+\phi) \right], \tag{3}$$

where z_f is the focus, ** represents the 2-D convolution, and the system effects $s(\cdot)$ and $n_e(\cdot)\sin(\cdot)$ are separable functions.

In our previous paper,[36] a lateral-only deconvolution was performed in the RF domain; however, to deconvolve the image in the axial direction, we face the choice of representing the signal as RF or in-phase quadrature (IQ): a bandpass versus low-pass quadrature pair. Theoretically, as long as the corresponding Z-transform has no zeros lying on the unit circle, either representation can produce a stable inverse. However, the IQ data have the advantage of requiring a lower Nyquist frequency. Furthermore, the baseband Gaussian (or related envelope shapes) from our previous work fits conveniently into our processing framework in that both generate stable inverse filters and perform coherent deconvolution. Thus, we choose to work with the I and Q pair for inverse filtering. Note that the IQ demodulation is performed in the axial direction, thus it does not significantly change the signal in the lateral direction in terms of the lateral PSF. Therefore, the deconvolution for both dimensions is performed in the IQ data domain. Below, starting from the RF data representation of the axial PSF, we analyze the details of the 2-D deconvolution in the IQ data domain.

Based on the model in Eq. (3), if we substitute z with $z = ct/2$, and then take the Fourier transform (laterally with respect to x and axially with respect to t), the spectrum of the received RF data in the frequency domain $\hat{R}(u,f)$ is equal to

$$\hat{R}(u,f) = \frac{j}{2} R(u,f) S(u) [E(f+f_0) - E(f-f_0)] \mathbf{e}^{jf\phi/f_0}, \tag{4}$$

where $R(u,f)$, $S(u)$, and $E(f)$ are the Fourier transforms of $r(x,t)$, $s(x/\lambda z_f)^2$, and $n_e(t)$, respectively, and $f_0 = \frac{kc}{2\pi}$ is the center frequency. Note that for the remainder of this paper, the axial depth z and the time t are interchangeable by the relationship $z = ct/2$.

To generate the IQ data, the RF data are multiplied by a complex signal $\mathbf{e}^{j2\pi f_0 t}$. This downmixing process gives a signal of

$$\hat{R}_{dm}(u,f) = \frac{j}{2} R(u,f+f_0) S(u) [E(f+2f_0) - E(f)] \mathbf{e}^{j(f+f_0)\phi/f_0}. \tag{5}$$

After low-pass filtering with a gain of 2, the spectrum of the baseband IQ data is generated as

$$\hat{R}_{IQ}(u,f) = -j[S(u)E(f)][R(u,f+f_0)\mathbf{e}^{j(f+f_0)\phi/f_0}]. \tag{6}$$

Going back to the spatial domain, the baseband IQ data become

$$\hat{r}_{IQ}(x,z) = -j[s(x/\lambda z_f)^2 n_e(2z/c)] ** [\mathbf{e}^{-j2kz} r(x, z+\phi/2k)]. \tag{7}$$

In conventional ultrasound imaging, the absolute value of the IQ data, denoted as

$$\hat{r}_{\text{disp}}(x,z) = |\hat{r}_{IQ}(x,z)| = |[s(x/\lambda z_f)^2 n_e(2z/c)] ** [\mathbf{e}^{-j2kz} r(x, z+\phi/2k)]|, \tag{8}$$

is displayed as an ultrasound image after logarithmic compression. Note that because of the phase interference inside the absolute value symbol, the deconvolution may not be applied to the envelope image. However, if we deconvolve the IQ data before taking the absolute value with some bounded-input bounded-output (BIBO) stable inverse filters for the PSFs $s(\cdot)^2$ and $n_e(\cdot)$, the resulting image becomes

$$\hat{r}_d(x,z) = |-j\mathbf{e}^{-j2kz} r(x, z+\phi/2k)| = |r(x, z+\phi/2k)|, \tag{9}$$

where the resolution enhancement is achieved. Note that the term $\phi/2k$ is a constant shift in the axial direction. For the worst case where $\phi = \pm\pi$, this corresponds to an offset of a quarter of a wavelength. Nevertheless, this offset is consistent for the entire image, thus the relative positions and sizes of the imaged objects are preserved. Hence, it does not influence the image quality.

The functions and calculations in the convolution model discussed here are in the "continuous" domain. However, in digital imaging systems, signal processing is completed in the

"discrete" domain. For that reason, we examine the Z-transform requirements for a stable inverse filter.

2.2 *Stability Constraints for Symmetric Functions*

In theory, let us consider a discrete function $f[k]$, symmetric about a maximum at $k=0$, where $k \in [-n, n]$ and $k \in \mathbb{Z}$. This has a Z-transform

$$F(z) = \sum_{k=-n}^{n} f[k] z^{-k}. \tag{10}$$

Note that in this section, z is the complex variable of the Z-transform, not the depth coordinate. The roots of $F(z)=0$ are the poles of the inverse filter of the discrete samples $\{f[k], k \in [-n, n]\}$.To have a stable inverse filter, the roots cannot be located on the unit circle to avoid singularity.

As shown in Ref. 36, $F(z)=0$ can be reformulated as $g(y) = \sum_{k=0}^{n} b_k y^k = 0$, if we set $y \triangleq z + (1/z)$, where $\{b_k\}$ is the coefficients of the polynomial. It was also shown that the "master constraint" for symmetric stabilized beam patterns is $|y_0| > 2$, where $y_0 \in \{y : g(y) = 0, y \in \mathbb{R}\}$, which enables the use of many classical root-testing methods. These additional theoretical considerations to further access the zeros of $g(y)$ include the Eneström–Kakeya theorem[42] and the Jury stability criterion.[43] Within these constraints lie some subsets of sampled beam patterns that have stable inverses.

3 Examples

In this section, examples are given to show that stable inverse filters exist for PSFs in both the lateral and the axial directions.

3.1 *Lateral Beam pattern: Broadband Gaussian Model*

In our previous paper,[36] we showed that the lateral focal beam pattern from the transducer with the Gaussian apodization function might be modeled as

$$s_{bG}(x) = \frac{\sqrt{\frac{\pi}{2}} f_0 \exp\left(-\frac{D^2 x^2}{2D^2\sigma_l^2 + B^2 x^2}\right)\left\{\operatorname{erf}\left[\frac{2\sqrt{2}}{B\sqrt{\frac{1}{\ln 2}\left(\frac{B^2 x^2}{D^2\sigma_l^2}+1\right)}}\right]+1\right\}}{\sqrt{\frac{x^2}{\sigma_l^2}+\frac{D^2}{B^2}}}, \tag{11}$$

where f_0 and B are the center frequency and the bandwidth of the transducer, respectively, σ_l is the standard deviation of the Gaussian apodization function in the transducer face, x is the lateral coordinate at focal depth, $\operatorname{erf}(\cdot)$ is the error function, and the constant $D = 4\sqrt{\ln 2}$. The stability constraint for a nine-point (denoted as $n_s = 9$, where n_S is the number of samples) discrete function sampled from this broadband Gaussian model with 50% bandwidth was given as

$$\Delta x > 0.775\sigma_l, \tag{12}$$

where Δx is the discrete sampling interval. As an example, a nine-point sampled function with $\Delta x = 1.1\sigma_l$ was analyzed in the Z-plane where all zeros in the Z-plane diagram were located away from the unit circle, thus generating a stable inverse filter. Similarly, stable inverse filters were also found for the five- and the seven-point samples from well-truncated Gaussian apodization functions.

3.2 *Axial Gaussian Envelope*

In simulations, a Gaussian function may be a popular but simple model for the axial pulse envelope $n_e(t)$. Based on the analysis in Sec. 3.1, stable inverse filters are needed for $n_e(t)$. It was previously shown that in Ref. 36, the stability constraint for the Gaussian function of the form

$$C \exp\left(-\frac{x^2}{2\sigma_0^2}\right) \tag{13}$$

was given by

$$\Delta x > 0.704\sigma_0. \tag{14}$$

As an example, a nine-point discrete function sampled from a Gaussian function with $\Delta x = 0.9\sigma_0$ was analyzed in the Z-plane where all zeros in the Z-plane diagram were located away from the unit circle, thus generating a stable inverse filter. Therefore, the previous stability analysis of the Gaussian function for the lateral direction can be utilized directly for the deconvolution of the baseband Gaussian envelope in the axial direction.

3.3 *Other Practical Axial Stabilized Pulses*

In general, controlling the shape of the axial PSF exactly is not a trivial task. In the lateral direction, the PSF can be predicted relatively easily using the Fourier transform of the apodization function.[44–46] Axially, the axial PSF is determined by the impulse responses of the transducer and the excitation signal, and is influenced by to the mechanics of the transducer, e.g., center frequency and damping. As studied in Ref. 47, to generate a specific transmitting waveform, the impulse response of the transducer was first estimated by solving an inverse problem through eight transmit/receive experiments, and then the tri-state excitation signal was solved according to the desired waveform.

A simpler way to obtain the axial PSF is to estimate the axial PSF of the transducer. For example, Jensen and Leeman[48] proposed a cepstrum-based estimation approach derived from homomorphic filtering, where the minimum phase of the pulse was assumed. In practice, however, it is better to use a parameterized model. This is because the shape of the pulse changes with depth, and frequency-dependent attenuation is expected.[48] The adaptiveness and flexibility of the parameterized model can take care of the shift-variant characteristics of the PSF in the practical imaging environment, where the pulse shape distorts during propagation.

To parameterize the axial PSF, the shape of the actual axial PSF should be reviewed. A typical two-way response of the ultrasound imaging system in the axial direction consists of several wavelengths, and its envelope is characterized by a relatively sharp initial rise around 0.2 μs, followed by a relatively smoother fall-off from the peak. Denoted as $p_a(t)$, this shape was modeled in Ref. 38 as a square root multiplied by a Gaussian function of time

$$p_a(t) = \sqrt{t}\, \exp[-(t-\tau)^2/2\sigma_a^2]\, \operatorname{UnitStep}(t), \tag{15}$$

where τ and σ_a are the mean and the standard deviation of the Gaussian function, respectively. Another model can be found in Ref. 49, which may be reformulated as

$$p_a(t) = t^3 \exp(-t^2/2\sigma_a^2)\,\mathrm{UnitStep}(t). \tag{16}$$

All these models share the form of the product of a polynomial and a Gaussian function, which can be modeled more generally as

$$p_a(t) = t^a \exp[-(t-\tau)^b/2\sigma_a^2]\,\mathrm{UnitStep}(t), \tag{17}$$

where the exponents a and b may be any real numbers. As an example, the model with $a = b = 2$ is used such that

$$p_a(t) = t^2 \exp[-(t-\tau)^2/2\sigma_a^2]\,\mathrm{UnitStep}(t). \tag{18}$$

To validate this model, the echo from the flat surface of a homogeneous gelatin phantom was recorded and curve-fitted. The phantom was immersed in water, and an ATL L7-4 transducer (Philips Healthcare, Andover, Massachusetts) with a center frequency of 5 MHz was placed with its axial direction perpendicular to the surface of the phantom. The distance from the transducer to the surface of the phantom was 2 cm, which is also where the focus of the transducer was located. The measured echo and the curve-fitted signal are shown in Fig. 1. A similar shape resulted for the situation when the distance and the focus were both 5 cm. The model in Eq. (18) was fitted as

$$p_a(t) = t^2 \exp[-(t-0.2017)^2/2/0.2235^2]\,\mathrm{UnitStep}(t). \tag{19}$$

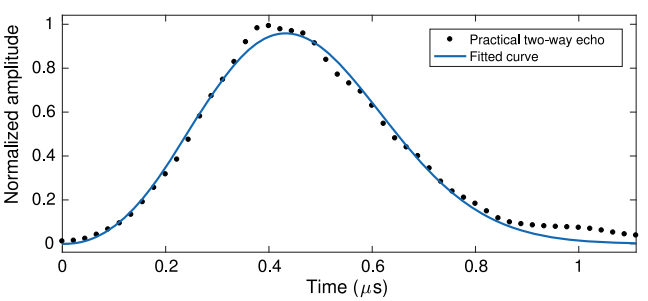

Fig. 1 Pulse-echo envelope (axial PSF) measured from the flat surface of a homogeneous gelatin phantom using L7-4 transducer. The samples are curved-fit into the model in Eq. (18).

The resulting goodness of fit was: sum of squared errors: 0.05166, coefficient of determination (R-square): 0.9909, adjusted R-square: 0.9906, and root mean squared error: 0.03281. Note that although a and b are treated here as hyperparameters, they may also be parameters and take part in the curve-fitting estimation.

Based on the model in Eq. (19), we can generate inverse filters that are stable and useful for the deconvolution in the axial direction. Figure 2 shows a stable inverse filter and the Z-plane plot from nine samples of the curve-fitted model. The samples are downsampled with a ratio of 10 from the raw data where the sampling frequency is 16 samples per period. The stability of the inverse filter is shown by the positions of the zeros that are away from the unit circle in the Z-plane diagram. A family of inverse filters may be generated by adjusting the parameters τ and σ_a in the model.

4 Practical Filtering Issues

In the previous paper,[36] we listed six practical issues for lateral-only deconvolution; they are the spatial variance of the PSF, the need for downsampling the original image data, parameterization of the inverse filters, conditioning kernel for dealing with noise, the cancellation of the quadratic phase term for the lateral PSF, and the coherent deconvolution for subinteger shifts. The first four are more general issues, and the solutions to those issues still apply to the axial direction in 2-D deconvolution. The previous one-dimensional (1-D) coherent deconvolution framework can be extended to the 2-D data; a detailed discussion is given below. In addition, the demodulation process that generates the IQ data is also investigated.

4.1 *Coherent Deconvolution with Inverse Filter Banks for Subinteger Shifts*

The coherent deconvolution was introduced to deal with the scatterers located among the sampled positions. In practice, a bank of five inverse filters generated from both the centered and shifted sampled functions are used for the deconvolution. This produces five intermediate deconvolution results, from which the candidate with the minimum absolute values is selected as the final output.

Assuming the separability of the lateral and the axial dimensions in the PSF, a coherent deconvolution may be performed in both dimensions sequentially, termed as "sequential coherent deconvolution." Specifically, if there are five inverse filters designed for each dimension, then the sequential application

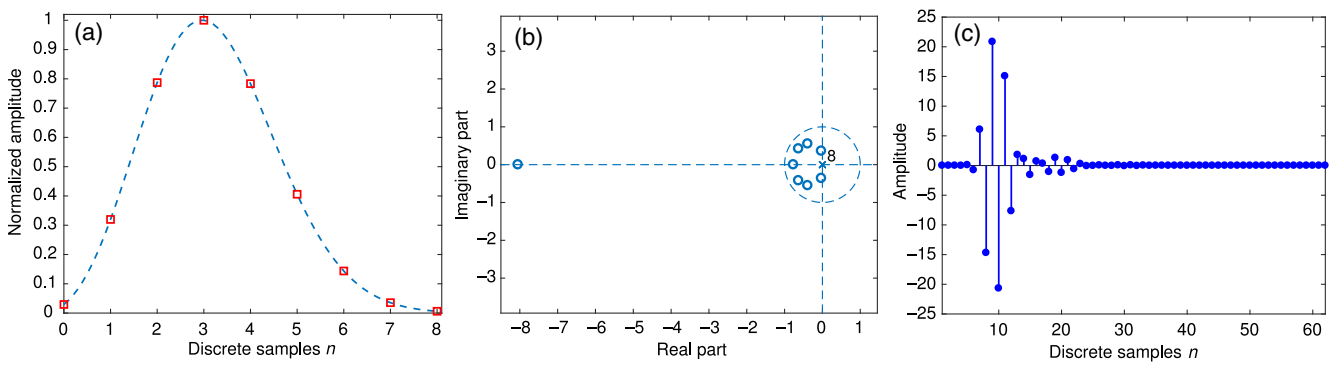

Fig. 2 (a) A nine-point discrete function sampled from the axial PSF model in Eq. (19). (b) The zeros of the Z-transform are located away from the unit circle, resulting in (c) a stable inverse filter.

of the inverse filters in both directions will produce 25 deconvolution results as candidates for the final image. Note that it does not matter whether the axial inverse filters or the lateral is applied first, because they are all linear operations.

In the IQ data domain, where data are composed of complex numbers, there are two methods to choose the best candidate. The first method is essentially the same as that used in the lateral-only deconvolution, i.e., picking the complex candidate with the minimum modulus (the "joint" method). The other method is to treat the real and imaginary parts separately (the "separate" method). The separate method first selects the I part with the minimum absolute value and the Q part in the same way, combines the two parts, and then takes the magnitudes of the selected IQ minima for image display.

Other than the two methods introduced above, the harmonic mean of the intermediate deconvolution results may also be chosen as the final output. The major feature is that its output, when compared to that of conventional averaging, is closer to the smallest values among the inputs. The harmonic mean w_{hm} of a set of positive numbers $w_1, w_2, \cdots, w_n$ is defined as

$$w_{\text{hm}} = \frac{n}{\sum_{i=1}^{n} \frac{1}{w_i}}. \tag{20}$$

There are also two ways to apply the harmonic mean method on the IQ data candidates: either taking the harmonic mean of the magnitude of the IQ data directly or treating the real and imaginary parts separately. Unlike the minimum-picking method, which always picks the candidate with the smallest absolute value, the harmonic mean of a set of numbers gathers information from all the inputs. Hence, the output image depends on which portion of the candidates is used. In practice, the smallest n_{hm} number of candidates in terms of absolute values may be used as the input of the harmonic mean. In that sense, the number n_{hm} may serve as a potential parameter for image display.

4.2 *Center Frequency in In-Phase Quadrature Data Demodulation*

The downmixing step in the generation of the IQ data requires knowledge of the center frequency. Due to frequency-dependent attenuation of the wave during propagation, the effective center frequency is lower than the original specified in transmission. To deal with this downshifting of frequency, the effective center frequency is estimated as[50,51]

$$\overline{f_0} = \frac{\int_0^{+\infty} fP(f)\mathrm{d}f}{\int_0^{+\infty} P(f)\mathrm{d}f}, \tag{21}$$

where $P(f)$ denotes the power spectrum of the RF data. Note that in a practical ultrasound scanner, this downmixing process begins with a higher center frequency for the near-field, decreases with depth, and remains the same when it reaches some certain threshold depth.[52]

4.3 *Final Procedures*

To summarize, the processing steps that occur after the introduction of the IQ data representation of the image and the model-based axial deconvolution are:

1. Estimate the lateral PSF by substituting the parameters with the imaging settings into the broadband Gaussian model as in Eq. (11) or by experiment.
2. Estimate the axial PSF using the model in Eq. (18) or by experiment.
3. Design stable inverse filters for both the lateral and the axial directions from the corresponding centered PSFs and from subinteger shifts with appropriate downsampling ratios (DSR) and relaxations of σ_l and σ_a.
4. Perform B-mode imaging using a Gaussian apodization for the transducer (with quadratic phase compensated if necessary) and acquire baseband IQ data.
5. To perform deconvolution, first downsample the IQ data in both the axial and lateral directions. Then, for each subgroup of IQ data, perform the sequential coherent deconvolution in both the lateral and the axial directions using the designed inverse filters with the conditioning kernel if necessary. Then, interleave the downsampled results.
6. Optionally, apply a median filter to the interleaved data to further reduce noise and any residuals of deconvolution.
7. Take the absolute values of the IQ data for envelope detection, if desired.

The procedures are also shown in Fig. 3.

5 Results and Discussion

The proposed method is implemented using Field II simulations in MATLAB® (The MathWorks, Inc., Natick, Massachusetts), and imaging of a tissue-mimicking phantom and the *in vivo* carotid artery using the Verasonics V1 scanner (Verasonics, Inc., Kirkland, Washington). The experiments were done using the ATL L7-4 and L12-5 38-mm transducers (Philips Healthcare, Andover, Massachusetts) with center frequencies of 5 and 7.5 MHz, respectively. The L7-4 transducer was modeled using Field II. On transmit, single focusing and a Gaussian apodization truncated in the 6σ range is applied with the quadratic phase compensated, while on receive, dynamic focusing is used with the same Gaussian apodization. The RF data were acquired at 16 samples per wavelength in the axial direction. In the lateral direction, the pixel spacing of the RF data is one-fifth of the pitch width based on denser pulse sequencing. In all cases, stable inverse filters were designed for both the axial and the lateral directions in advance based on the models with proper relaxation of the parameters. The conditioning kernel in the downsampled domain is used when necessary, and a small 5×5 median filter is applied twice in the interleaving domain before the envelope detection as a simple noise reduction step. All the ultrasound images are normalized to the maximum and displayed in 50-dB dynamic range. We first show a simulation result using Field II to validate the extension of the proposed deconvolution framework from 1-D to 2-D. After that, results utilizing stable inverse filters from the practical model for axial PSF were examined using the Verasonics scanner with tissue-mimicking phantom, followed by *in vivo* imaging of the carotid artery.

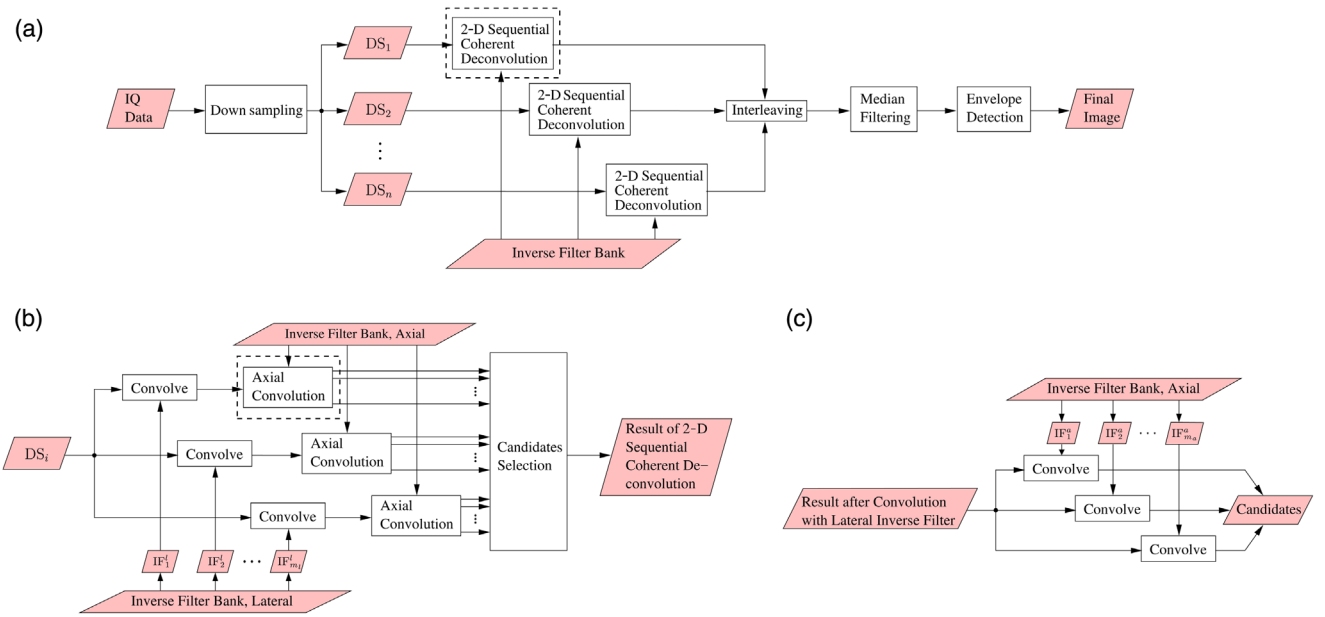

Fig. 3 Flow chart showing (a) overview of the processing procedures, (b) the details of the 2-D sequential coherent deconvolution box, and (c) the details of axial convolution box. DS_i is the i'th downsampled IQ data; the inverse filter bank contains inverse filters (IF^l for the inverse filters designed for the lateral direction and IF^a for the axial direction) for discrete function sampled with subinteger shifts; and the candidates selection chooses the convolution result with methods including the minimum-picking method and the harmonic mean method.

5.1 *Field II Simulation*

The extension of the deconvolution framework to the axial direction was first verified using Field II simulation. The transducer is an ATL L7-4 linear transducer, and its impulse response is modeled as a Gaussian-modulated sine with 50% bandwidth, resulting in a simple Gaussian axial PSF in accordance with Sec. 3.2. The number of active transducer elements is 64. The depth of the phantom is from 45 to 55 mm. It consists of, from left to right, a blood vessel, an anechoic cyst, individual scatterers, and a hyperechoic lesion. Specifically, the diameters of the inner and the outer walls of the blood vessel are 3 and 3.5 mm, respectively; the lateral distance between the two scatterers at the same depth is 1.5 mm; both the cyst and the lesion share the same diameter of 5 mm. Five pairs of individual scatterers are placed at the depths from 46 to 54 mm with an axial step of 2 mm. The lateral distance between each pair is 1.5 mm. Furthermore, three more pairs of single scatterers are added into the simulated phantom such that at the depths of 46, 50, and 54 mm, there are scatterers separated by one wavelength (at frequency of 5 MHz) axially for evaluating the performance of the axial resolution enhancement. The original B-mode image simulated is shown in Fig. 4(a). As can be seen in the figure, in the region of the individual scatterers, five bright blurs are found, and the details of the scatterers underneath cannot be discerned. Figure 4(b) shows the result if the boxcar apodization is used. Although the lateral resolution is better, the axial scatterer pairs still cannot be distinguished. The sidelobes brought by the boxcar apodization are also seen.

Following the procedures of the proposed framework, stable inverse filters in both axial and lateral directions were generated and used for deconvolution. Inverse filters in the lateral direction were generated from the broadband Gaussian model with DSR equal to 10 and $n_s = 9$. For the axial direction, five stable inverse filters were calculated from the corresponding Gaussian envelope with a DSR of 15 and $n_s = 9$. The σ_l and σ_0 were relaxed by a factor of 0.95 and 1.15, respectively, for the lateral and the axial direction. The deconvolution starts with the application of the lateral inverse filters, followed by the five inverse filters in the axial direction, creating 25 deconvolution results. A conditioning kernel of [1, 1] is convolved in the axial direction.

Figures 4(c) and 4(d) show the results of the raw separate and the raw joint methods, respectively. In both images, the originally blurred scatterers are resolved both axially and laterally as seen from the increase of the diameter of the cyst, the decrease of the diameter of the lesion, and the separation of the scatterers. Specifically, for Figs. 4(a) and 4(c), the size of the cyst in diameter (lateral × axial) is increased from 3.43 mm × 4.36 mm to 4.74 mm × 4.77 mm, and the blood vessel wall is seen much more clearly in Fig. 4(c) than in the original image. The size of the inner blood vessel wall, which is designed to be 3 mm in diameter, is opened from barely visible to about 2.07 mm × 2.20 mm. The separate method IQ demonstrates high performance in resolving the single scatterers but suffers seriously from the erosion of the speckle regions, as many pixels drop below the −50-dB dynamic range of the image display. On the other hand, the joint method [Fig. 4(d)] provides a better speckle region while increasing the side-lobes and residuals that blur the objects of interest; this is especially evident in the long streaks in the axial direction of the single scatterers.

Figures 4(e) and 4(f) show the harmonic mean images with $n_{\text{hm}} = 4$ for both the separate and the joint approaches. From these figures, it is seen that the joint images have better speckle uniformity, while the separate images have better resolution and fewer residuals. Further, the harmonic mean images, to some extent, balance the trade-off between the resolution performance and the speckle erosion when compared to their minimum-picking method counterparts. Last, it should be noted that all the intermediate deconvolution results are converted to their

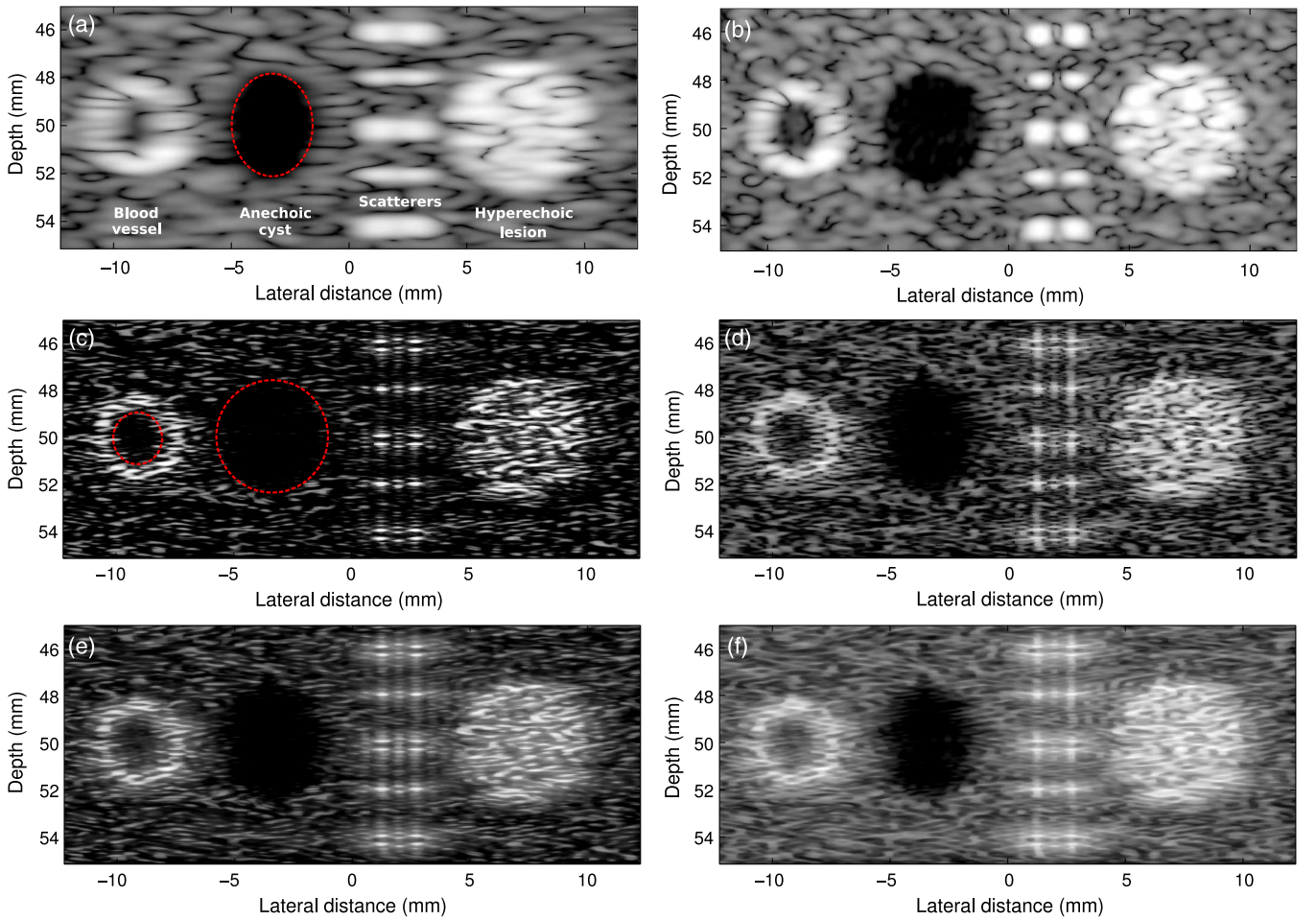

Fig. 4 Image simulated from Field II with (a) Gaussian and (b) boxcar apodization. The result from the Gaussian apodization is processed with a 2-D deconvolution using (c) the separate and (d) the joint minimum-picking methods, and (e) separate and (f) joint harmonic mean calculation with $n_{hm} = 4$. The red circles indicate apparent lumen boundaries.

absolute values before computing the harmonic mean, which makes the result of the harmonic mean all positive numbers. As a result, the median filtering step described in the procedure in Sec. 4.3 is applied to the positive values that would otherwise be positive and negative if the minimum-picking method was used. This may explain why the images resulting from the harmonic mean method appear more "filled-in" than those from the minimum-picking methods.

The resolution of the original images and processed result using the separate minimum-picking method was examined in more detail. Figure 5 compares the axial cuts at $x = 1.5$ mm across the individual scatterers separated by about 0.3 mm at the depth around 50 mm. There is a tiny difference between cuts from images simulated with Gaussian and boxcar apodization, neither of which can resolve the scatterers. In contrast, the scatterers are clearly resolvable in the axial cut from the image processed with the separate method. The gain of the resolution can also be evaluated through the normalized 2-D autocorrelation of the envelope. The −6-dB width of the autocorrelation function is narrowed by 8.75 and 20.5 times in the lateral and axial directions, respectively.

In conclusion, the results from the above Field II simulation example validate the extension of the proposed deconvolution framework from 1-D (lateral only) to 2-D (axial and lateral).

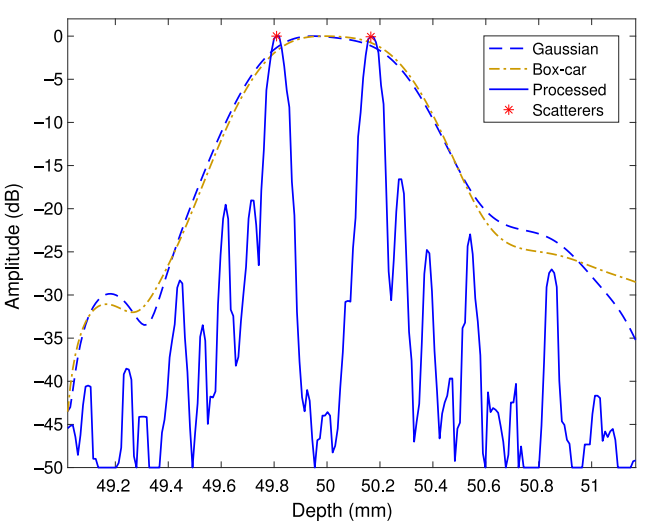

Fig. 5 Comparison of envelopes along the axial lines at $x = 1.5$ mm across the images at depth of 50 mm showing the resolution of two individual scatterers in the axial direction. The data are from the images with Gaussian function apodization, with boxcar function apodization, and with Gaussian function apodization after deconvolution.

The results also verify the theoretical analysis regarding deconvolution using the IQ data described in Sec. 2. Further, since only one bank of inverse filters (designed for the depth of 50 mm) is used, the result also shows the tolerance of the inverse filters for depths that are off-focus to some extent.

5.2 *Imaging of a Tissue-Mimicking Phantom*

The region in the ATS 535 QA ultrasound phantom, (ATS Laboratories, Inc., Bridgeport, Connecticut) which contains a small cyst with a nominal diameter of 4 mm was imaged using the Verasonics scanner with an ATL L7-4 transducer with 64 active transducer elements. This image was purposefully made to have high noise by utilizing low transmit power with high receive gain. The lateral inverse filters generated from the broadband Gaussian model were used for deconvolving the IQ data in the lateral direction while in the axial direction, inverse filters were generated from the model in Eq. (19). The parameters σ_l and σ_a were both relaxed by 0.95, and a conditioning kernel of [1/2, 1, 1/2] was applied axially.

Figure 6 shows from top to bottom, the original image and the processed images. Specifically, Fig. 6(b) shows the result after the lateral-only deconvolution and Fig. 6(c) with 2-D deconvolution. The raw separate method is used here for Figs. 6(b) and 6(c). The lateral opening of the cyst in the images from top to bottom increases from 1.50 to 2.94 to 3.24 mm as illustrated by the red ellipses, and axially, the diameter increases from 2.60 to 2.89 to 3.33 mm. The numbers show a major enhancement for the resolution after the deconvolution in each direction. The reason for the further opening-up of the cyst in the lateral direction after the introduction of an axial deconvolution is that the increased number of candidates (from 5 for 1-D to 25 for 2-D) enables the final output to be more likely to catch a candidate with magnitude closer to zero.

5.3 *In Vivo Imaging of the Carotid Artery*

In vivo imaging of the carotid artery was also performed to comprehensively evaluate the performance of the proposed method. Figure 7(a) shows the original image of the carotid artery together with the thyroid of a healthy adult imaged under the requirements of informed consent and the University of Rochester Institutional Review Board. Stable inverse filters in both directions were found and applied onto the original IQ data for sequential coherent deconvolution. The parameters σ_l and σ_a were relaxed by 1.05 and 0.8, respectively. A conditioning kernel of [1, 1] was applied laterally while in the axial direction, a kernel of [1/2, 1, 1/2] was applied. Note that the separate harmonic mean method with $n_{\mathrm{hm}} = 7$ was used to preserve the homogeneity of the speckle region. The processed image is shown in Fig. 7(b), where the vessel wall of the carotid artery is better defined, and the speckle pattern of the thyroid region becomes finer as the −6-dB width of the autocorrelation function of the speckle region is narrowed by 4.5 and 5.1 times in the lateral and axial directions, respectively.

2-D deconvolution can also be used to help measure the intima-media thickness (IMT) of the carotid artery. The IMT measures the distance between the lumen-intima and the media-adventitia, and marks subclinical atherosclerosis.[53] Because the thickness is indicated as the length in the axial direction, the IMT measurement is expected to benefit from axial resolution enhancement.

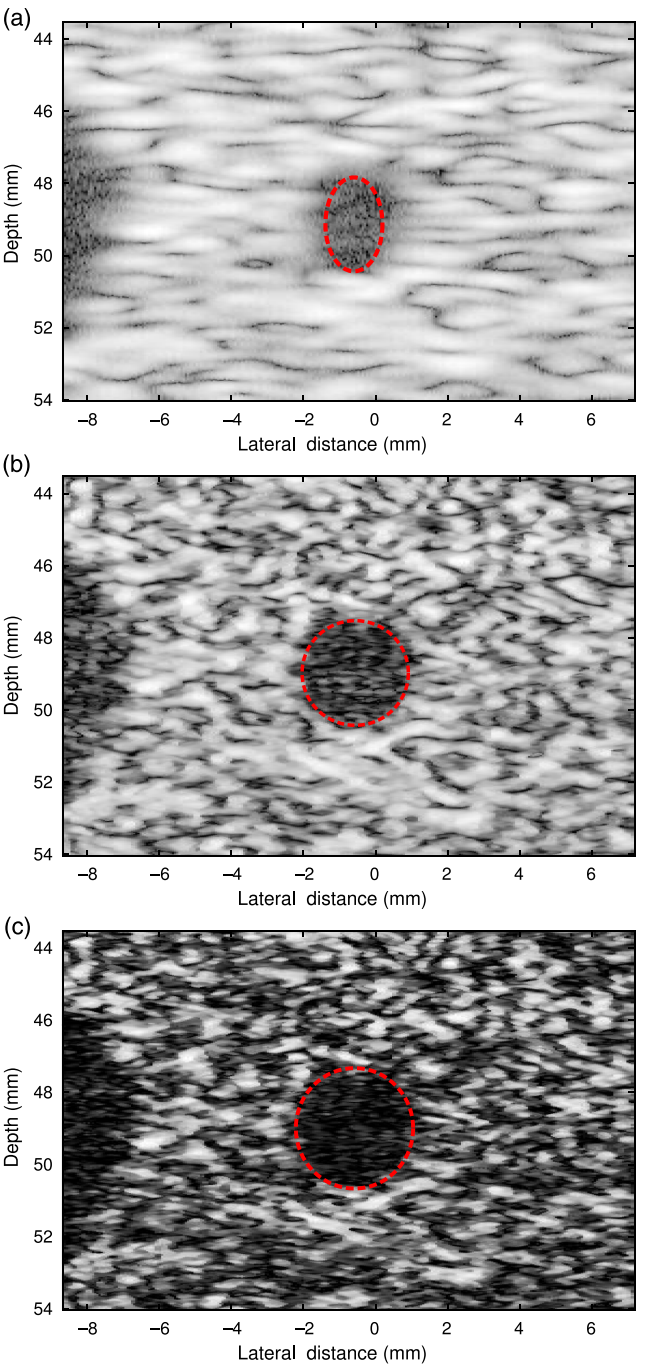

Fig. 6 A 2-D deconvolution of a cyst phantom under high noise conditions. (a) The original image, (b) the resulting image after 1-D (lateral) deconvolution, and (c) the resulting image after 2-D (axial and lateral) deconvolution.

Figure 8(a) shows a longitudinal view of the same carotid artery. The image data were generated using the Verasonics scanner with an L12-5 38-mm transducer with 48 active elements. Fewer active elements were used so that the F number is maintained above 2. The red arrows point out the position of the blood-intima interface of the IMT measurement. Based on the proposed deconvolution framework in the IQ data domain, stable inverse filters were generated and used for deconvolution. A joint minimum-picking method was used for candidate selection. The parameters σ_l and σ_a were both relaxed by 0.95.

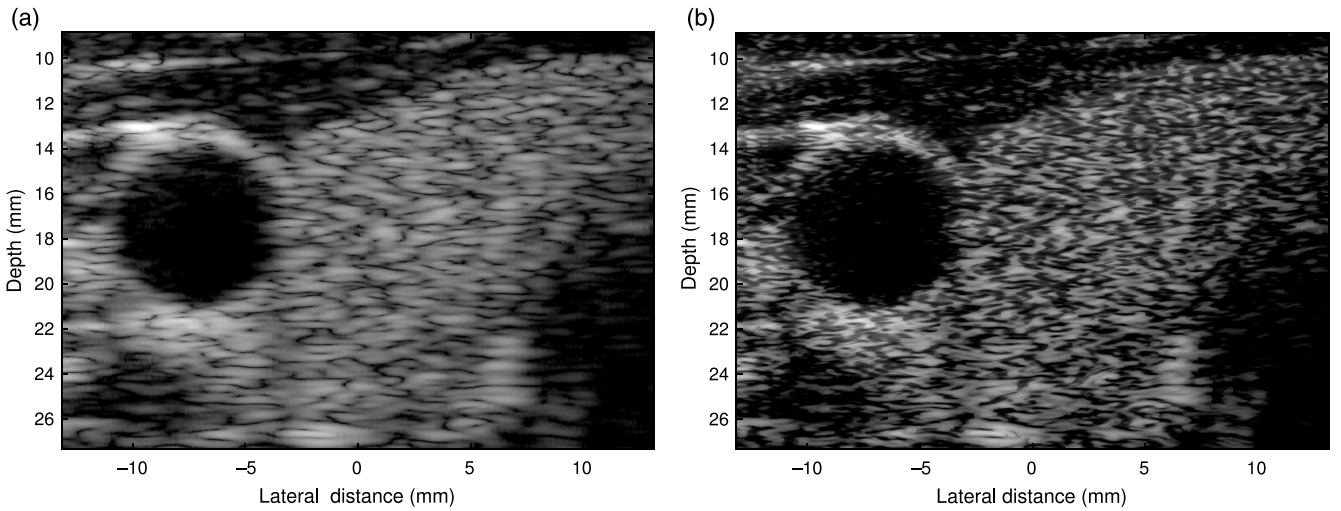

Fig. 7 A 2-D deconvolution of an image from *in vivo* scan, which contains the carotid artery and the thyroid. (a) The original image and (b) the image after deconvolution.

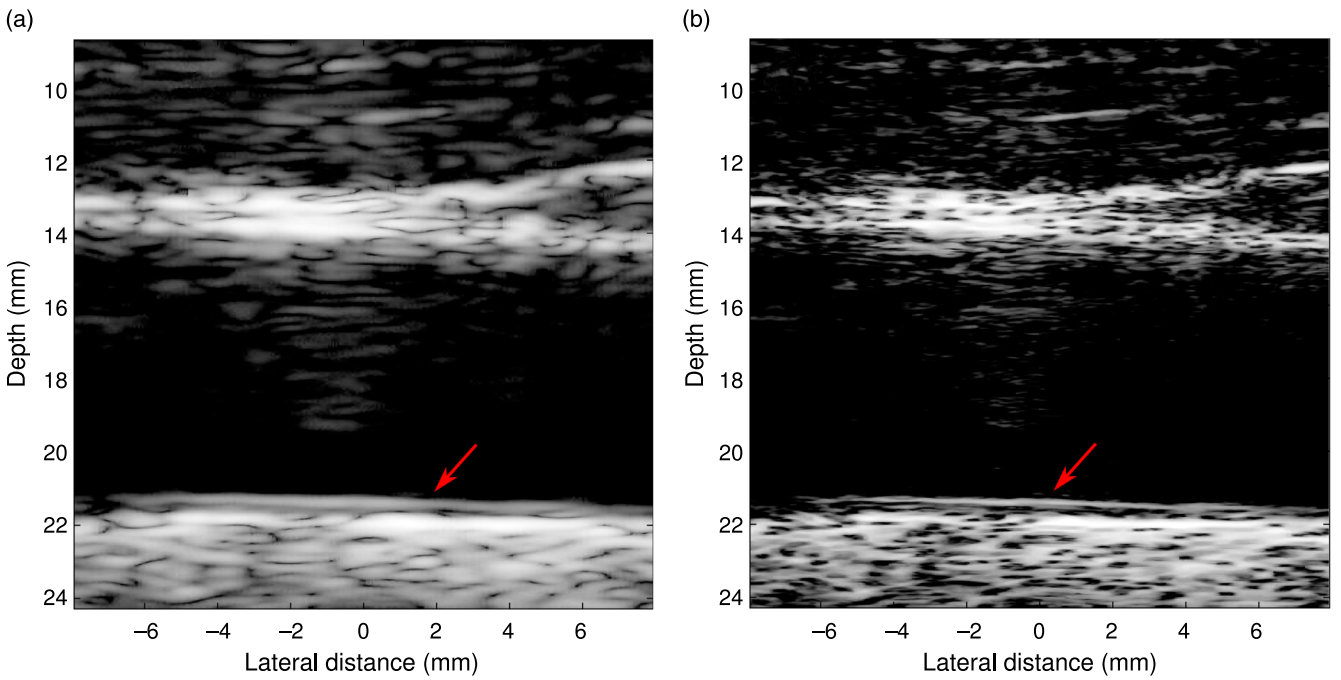

Fig. 8 A 2-D deconvolution of a carotid artery image. (a) The original image and (b) the image after deconvolution. The arrows point to the blood-intima interface, which is related to the IMT measurements.

A conditioning kernel of [1, 1] was applied laterally while in the axial direction, a kernel of [1/2, 1, 1/2] was applied. The resulting image after applying the 2-D axial and lateral coherent deconvolution is shown in Fig. 8(b), where sharper interfaces of lumen-intima and media-adventitia are shown. The sharpening is also shown in Fig. 9, where axial cuts going across both interfaces (depth from 21.2 to 22.0 mm) in Figs. 8(a) and 8(b) at a lateral distance equal to about −1 mm are shown.

5.4 *Further Discussion*

The erosion in the speckle region is inherent in the coherent deconvolution, because the candidates with the smaller, if not the minimum, absolute values are selected. This gives rise to reduced image intensity (darker image) away from strong scatterers. The regions where sparse single scatterers are present benefit from such characteristics because the relatively high intensity of any strong scatterers is maintained, whereas for regions that are more homogeneous, such erosion increases the size of dark channels within a speckle pattern. Therefore, there is always a trade-off between having better resolution for the highly reflecting scatterers and maintaining the smoothness of the speckle region. A harmonic mean calculation has been tested as a substitute for the minimum-picking method in finding a balance, but further investigation is needed.

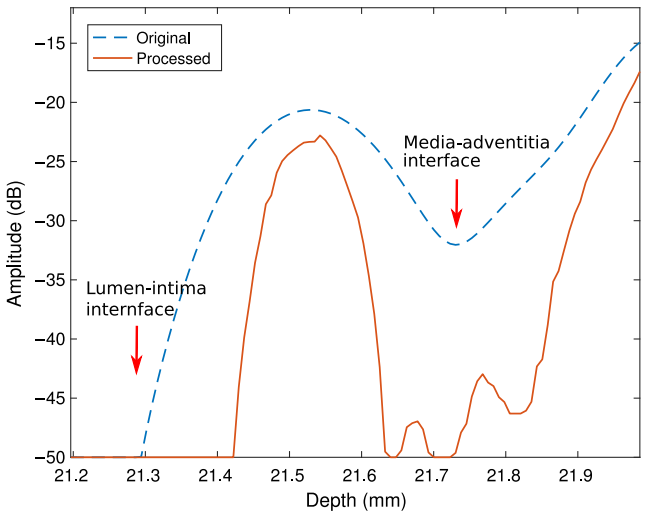

Fig. 9 Comparison of the axial cuts going across both interfaces (depth from 21.2 to 22.0 mm) in Figs. 8(a) and 8(b) at lateral distance equal to about −1 mm before and after inverse filtering. The arrows point out the position of lumen-intima and media-adventitia interfaces. The amplitude in dB is normalized to the maximum amplitude of the image that each cut belongs to.

We note that for deep-seated organs, depth-dependent attenuation, wavefront aberration, and nonlinear propagation may become more serious and can result in the distortion of the PSF, degrading the quality of resolution enhancement. Nevertheless, in our framework, the inverse filters may be changed by relaxing the parameters in our model (σ_l and σ_a) within the constraints of stable inverse solutions. If an image quality or metric is chosen, the "optimal" value of the parameters can be selected accordingly for a practical imaging condition. The image quality metrics include but are not limited to: visual criteria from a sonographer, flatness of the power spectrum density,[54] and resolution gain (using width of the autocovariance function of the RF/envelope data,[25] width of the autocorrelation function of the envelope,[2,29,30,55] or width of the envelope of the autocovariance of the RF data[27]).

The stability criterion of the inverse filters in this work requires a rather low sampling frequency, causing aliasing that hinders the performance of deconvolution. Coherent deconvolution has been introduced to address this issue, combining multiple intermediate deconvolution results of low quality to achieve an enhanced resolution. Furthermore, the stability criterion itself might be improved so that better intermediate images can be obtained. To be specific, the BIBO stability requires that the sampled function has no zeros on the unit circle of the Z-plane, which is equivalent to the requirement that its discrete-time Fourier transform (DTFT) has no zeros. Take the Gaussian function of the form in Eq. (13) as an example. Without the loss of generality, for a sampling internal of $\Delta x = 1$, its DTFT spectrum is

$$C\mathbf{e}^{-\sigma_0\omega^2}\sqrt{2\pi\sigma_0}\vartheta_3(j\pi\omega\sigma_0, \mathbf{e}^{-2\pi^2\sigma_0}), \tag{22}$$

where $\vartheta_3(\cdot,\cdot)$ is a Jacobi theta function[56] and ω is the variable denoting the angular frequency. Equation (22), as a DTFT spectrum, has a period of 2π and never goes to zero, although its minimum at $\omega = \pm n\pi$, $n \in Z^+$, approaches zero asymptotically as the sampling frequency increases. In comparison, sampling a PSF with a finite number of samples leads to a convolution between the original DTFT spectrum and a sinc function, which may give rise to zeros both on the spectrum and on the unit circle. It is noted that as the number of samples increases toward infinity, the stability criterion such as Eq. (14) may become looser. It is expected that this will allow higher sampling frequency and lower DSR, which might further enhance the performance of the deconvolution with the possible trade-off of noise amplification.

6 Conclusion

The previously proposed deconvolution framework has been extended to the 2-D situation where both the axial and lateral deconvolution is considered. A mathematical derivation based on the classical convolution model of ultrasound imaging has shown that resolution enhancement can be achieved by deconvolving the ultrasound images in the IQ data domain using stable inverse filters of the envelope of the axial PSF. Within the updated procedures, the lateral deconvolution is conducted along with its axial counterpart through sequential coherent deconvolution. Examples that apply the proposed method to images from both Field II simulation and the Verasonics scanner have shown enhanced resolution in both dimensions by resolving individual scatterers, opening the anechoic cyst, and sharpening the carotid artery images. The resolution seen is enhanced by as many as 8.75 and 20.5 times in the lateral and the axial directions, respectively, evaluating the −6-dB width of the autocorrelation of the envelope images.

Disclosures

No conflicts of interest, financial or otherwise, are declared by the authors.

Acknowledgments

This work was supported by the University of Rochester and the Hajim School of Engineering and Applied Sciences.

References

1. S. H. C. Ortiz, T. Chiu, and M. D. Fox, "Ultrasound image enhancement: a review," *Biomed. Signal Process. Control* **7**(5), 419–428 (2012).
2. O. Michailovich and A. Tannenbaum, "Blind deconvolution of medical ultrasound images: a parametric inverse filtering approach," *IEEE Trans. Image Process.* **16**(12), 3005–3019 (2007).
3. G. Trahey et al., "A quantitative approach to speckle reduction via frequency compounding," *Ultrason. Imaging* **8**(3), 151–164 (1986).
4. G. E. Trahey, S. Smith, and O. Von Ramm, "Speckle pattern correlation with lateral aperture translation: experimental results and implications for spatial compounding," *IEEE Trans. Ultrason. Ferroelect. Freq. Control* **33**(3), 257–264 (1986).
5. T. Gan et al., "The use of broadband acoustic transducers and pulse-compression techniques for air-coupled ultrasonic imaging," *Ultrasonics* **39**(3), 181–194 (2001).
6. B. Haider, P. A. Lewin, and K. E. Thomenius, "Pulse elongation and deconvolution filtering for medical ultrasonic imaging," *IEEE Trans. Ultrason. Ferroelect. Freq. Control* **45**(1), 98–113 (1998).
7. R. Y. Chiao, L. J. Thomas, and S. D. Silverstein, "Sparse array imaging with spatially-encoded transmits," *Ultrasonics Symp., Proc.*, pp. 1679–1682, IEEE, (1997).
8. F. Gran and J. A. Jensen, "Spatial encoding using a code division technique for fast ultrasound imaging," *IEEE Trans. Ultrason. Ferroelect. Freq. Control* **55**(1), 12–23 (2008).
9. J. A. Jensen et al., "Synthetic aperture ultrasound imaging," *Ultrasonics* **44**, e5–e15 (2006).
10. R. S. Shapiro et al., "Tissue harmonic imaging sonography: evaluation of image quality compared with conventional sonography," *Am. J. Roentgenol.* **171**(5), 1203–1206 (1998).

11. F. Tranquart et al., "Clinical use of ultrasound tissue harmonic imaging," *Ultrasound Med. Biol.* **25**(6), 889–894 (1999).
12. A. J. Devaney, "Super-resolution processing of multi-static data using time reversal and MUSIC," http://www.ece.neu.edu/fac-ece/devaney/preprints/paper02n_00.pdf (2000).
13. S. K. Lehman and A. J. Devaney, "Transmission mode time-reversal super-resolution imaging," *J. Acoust. Soc. Am.* **113**(5), 2742–2753 (2003).
14. A. J. Devaney, E. A. Marengo, and F. K. Gruber, "Time-reversal-based imaging and inverse scattering of multiply scattering point targets," *J. Acoust. Soc. Am.* **118**(5), 3129–3138 (2005).
15. C. Prada and M. Fink, "Eigenmodes of the time reversal operator: a solution to selective focusing in multiple-target media," *Wave Motion* **20**(2), 151–163 (1994).
16. C. Prada et al., "Decomposition of the time reversal operator: detection and selective focusing on two scatterers," *J. Acoust. Soc. Am.* **99**(4), 2067–2076 (1996).
17. L. Huang et al., "Detecting breast microcalcifications using super-resolution ultrasound imaging: a clinical study," *Proc. SPIE* **8675**, 867510 (2013).
18. Y. Labyed and L. Huang, "Ultrasound time-reversal MUSIC imaging of extended targets," *Ultrasound Med. Biol.* **38**(11), 2018–2030 (2012).
19. J. A. Jensen, "Deconvolution of ultrasound images," *Ultrason. Imaging* **14**(1), 1–15 (1992).
20. J. Gore and S. Leeman, "Ultrasonic backscattering from human tissue: a realistic model," *Phys. Med. Biol.* **22**(2), 317–326 (1977).
21. J. A. Jensen, "Ultrasound imaging and its modeling," in *Imaging of Complex Media with Acoustic and Seismic Waves*, M. Fink et al., Eds., pp. 135–166, Springer, Berlin, Heidelberg (2002).
22. J. A. Jensen, "A model for the propagation and scattering of ultrasound in tissue," *Acoust. Soc. Am. J.* **89**(1), 182–190 (1991).
23. J. Ng et al., "Modeling ultrasound imaging as a linear, shift-variant system," *IEEE Trans. Ultrason. Ferroelect. Freq. Control* **53**(3), 549–563 (2006).
24. R. J. Zemp, C. K. Abbey, and M. F. Insana, "Linear system models for ultrasonic imaging: application to signal statistics," *IEEE Trans. Ultrason. Ferroelect. Freq. Control* **50**(6), 642–654 (2003).
25. U. R. Abeyratne, A. P. Petropulu, and J. M. Reid, "Higher order spectra based deconvolution of ultrasound images," *IEEE Trans. Ultrason. Ferroelect. Freq. Control* **42**(6), 1064–1075 (1995).
26. P. Campisi and K. Egiazarian, *Blind Image Deconvolution: Theory and Applications*, CRC Press, Boca Raton, Florida (2007).
27. J. A. Jensen, "Real time deconvolution of in-vivo ultrasound images," in *2013 IEEE Int. Ultrasonics Symp. (IUS)*, pp. 29–32 (2013).
28. O. V. Michailovich and D. Adam, "A novel approach to the 2-D blind deconvolution problem in medical ultrasound," *IEEE Trans. Med. Imaging* **24**(1), 86–104 (2005).
29. T. Taxt and J. Strand, "Two-dimensional noise-robust blind deconvolution of ultrasound images," *IEEE Trans. Ultrason. Ferroelect. Freq. Control* **48**(4), 861–866 (2001).
30. C. Yu, C. Zhang, and L. Xie, "A blind deconvolution approach to ultrasound imaging," *IEEE Trans. Ultrason. Ferroelect. Freq. Control* **59**(2), 271–280 (2012).
31. O. Michailovich and D. Adam, "Phase unwrapping for 2-D blind deconvolution of ultrasound images," *IEEE Trans. Med. Imaging* **23**(1), 7–25 (2004).
32. T. Taxt, "Three-dimensional blind deconvolution of ultrasound images," *IEEE Trans. Ultrason. Ferroelect. Freq. Control* **48**(4), 867–871 (2001).
33. T. Taxt and G. V. Frolova, "Noise robust one-dimensional blind deconvolution of medical ultrasound images," *IEEE Trans. Ultrason. Ferroelect. Freq. Control* **46**(2), 291–299 (1999).
34. M. Blume et al., "A new and general method for blind shift-variant deconvolution of biomedical images," in *Int. Conf. on Medical Image Computing and Computer-Assisted Intervention*, pp. 743–750 (2007).
35. J. Ng et al., "Wavelet restoration of medical pulse-echo ultrasound images in an EM framework," *IEEE Trans. Ultrason. Ferroelectr. Freq. Control* **54**(3), 550–568 (2007).
36. S. Chen and K. J. Parker, "Enhanced resolution pulse-echo imaging with stabilized pulses," *J. Med. Imaging* **3**(2), 027003 (2016).
37. J. Kang et al., "Fast non-blind deconvolution based on 2D point spread function database for real-time ultrasound imaging," *Proc. SPIE* **8656**, 86560R (2013).
38. K. J. Parker, "Superresolution imaging of scatterers in ultrasound B-scan imaging," *J. Acoust. Soc. Am.* **131**(6), 4680–4689 (2012).
39. J. A. Jensen, "Simulation of advanced ultrasound systems using field II," in *IEEE Int. Symp. on Biomedical Imaging: Nano to Macro*, pp. 636–639 (2004).
40. J. A. Jensen, "Field: a program for simulating ultrasound systems," in *10th Nordibaltic Conf. on Biomedical Imaging*, pp. 351–353 (1996).
41. J. L. Prince and J. M. Links, "Ultrasound imaging systems," in *Medical Imaging Signals and Systems*, Pearson Prentice Hall, Upper Saddle River, New Jersey (2006).
42. V. V. Prasolov and D. Leites, *Polynomials*, Springer, Berlin (2004).
43. S. M. Shinners, *Advanced Modern Control System Theory and Design*, Wiley, New York (1998).
44. J. W. Goodman, *Introduction to Fourier Optics*, Roberts and Company Publishers, Englewood, Colorado (2005).
45. K. J. Parker, "Correspondence: apodization and windowing functions," *IEEE Trans. Ultrason. Ferroelect. Freq. Control* **60**(6), 1263–1271 (2013).
46. K. J. Parker, "Correspondence-apodization and windowing eigenfunctions," *IEEE Trans. Ultrason. Ferroelect. Freq. Control* **61**(9), 1575–1579 (2014).
47. J. A. Flynn et al., "Arbitrary waveforms using a tri-state transmit pulser," in *2013 IEEE Int. Ultrasonics Symp. (IUS)*, pp. 41–44 (2013).
48. J. A. Jensen and S. Leeman, "Nonparametric estimation of ultrasound pulses," *IEEE Trans. Biomed. Eng.* **41**(10), 929–936 (1994).
49. N. Zhao et al., "Blind deconvolution of medical ultrasound images using a parametric model for the point spread function," in *2016 IEEE Int. Ultrasonics Symp. (IUS)*, pp. 1–4 (2016).
50. B. A. Angelsen, "Instantaneous frequency, mean frequency, and variance of mean frequency estimators for ultrasonic blood velocity Doppler signals," *IEEE Trans. Biomed. Eng.* **BME-28**, 733–741 (1981).
51. C. Kasai et al., "Real-time two-dimensional blood flow imaging using an autocorrelation technique," *IEEE Trans. Sonics Ultrason.* **32**(3), 458–464 (1985).
52. BK Ultrasound, *IQ Demodulation*, http://www.ultrasonix.com/wikisonix/index.php/IQ_Demodulation#Down_Mixing (5 February 2017).
53. B. Coll and S. B. Feinstein, "Carotid intima-media thickness measurements: techniques and clinical relevance," *Curr. Atherosclerosis Rep.* **10**(5), 444–450 (2008).
54. D. Adam and O. Michailovich, "Blind deconvolution of ultrasound sequences using nonparametric local polynomial estimates of the pulse," *IEEE Trans. Biomed. Eng.* **49**(2), 118–131 (2002).
55. R. Morin et al., "Semi-blind deconvolution for resolution enhancement in ultrasound imaging," in *20th IEEE Int. Conf. on Image Processing (ICIP 2013)*, pp. 1413–1417 (2013).
56. E. T. Whittaker and G. N. Watson, *A Course of Modern Analysis*, Cambridge University Press, Cambridge, UK (1996).

Shujie Chen, MS, is a PhD candidate in the Department of Electrical and Computer Engineering at the University of Rochester. He earned his BS degree in communications engineering from Nanjing University of Posts and Telecommunications, Nanjing, China, in 2007, and his MS degree in electrical engineering from the University of Rochester in 2013. He interned with MathWorks in signal processing in the summer of 2016. His research interests are ultrasound imaging and image processing.

Kevin J. Parker, PhD, is the William F. May professor of engineering at the University of Rochester. He earned his graduate degrees from Massachusetts Institute of Technology and served at University of Rochester as department chair, director of the Rochester Center for Biomedical Ultrasound, and dean of engineering/applied sciences. He holds 25 US and 13 international patents (licensed to 25 companies), is a founder of VirtualScopics, and has published 200 journal articles. He is a fellow of IEEE, AIUM, ASA, and AIMBE.